The Meteoritical Society

Meteoritics & Planetary Science 48, Nr 10, 1757–1779 (2013)
doi: 10.1111/maps.12078

The Košice meteorite fall: Atmospheric trajectory, fragmentation, and orbit

Jiří BOROVIČKA[1*], Juraj TÓTH[2], Antal IGAZ[3], Pavel SPURNÝ[1], Pavel KALENDA[4], Jakub HALODA[5], Ján SVOREŇ[6], Leonard KORNOŠ[2], Elizabeth SILBER[7,8], Peter BROWN[7,8], and Marek HUSÁRIK[6]

[1]Astronomical Institute, Academy of Sciences of the Czech Republic, Ondřejov, CZ-25165 Czech Republic
[2]Faculty of Mathematics, Physics and Informatics, Comenius University, Mlynská dolina, Bratislava, SK-84248 Slovakia
[3]Hungarian Astronomical Association, MCSE, Pf. 148, 1300 Budapest, Hungary
[4]Institute of Rock Structure and Mechanics, Academy of Sciences of the Czech Republic, V Holešovičkách 41, Praha 8, CZ-18209 Czech Republic
[5]Czech Geological Survey, Geologická 6, Praha 5, CZ-15200 Czech Republic
[6]Astronomical Institute, Slovak Academy of Sciences, Tatranská Lomnica, SK-05960 Slovakia
[7]Department of Physics and Astronomy, University of Western Ontario, London, Ontario N6A3K7, Canada
[8]Centre for Planetary Science and Exploration, University of Western Ontario, London, Ontario N6A 5B7, Canada
[*]Corresponding author. E-mail: Jiri.Borovicka@asu.cas.cz

(Received 13 April 2012; revision accepted 17 November 2012)

Abstract–The Košice meteorite fall occurred in eastern Slovakia on February 28, 2010, 22:25 UT. The very bright bolide was imaged by three security video cameras from Hungary. Detailed bolide light curves were obtained through clouds by radiometers on seven cameras of the European Fireball Network. Records of sonic waves were found on six seismic and four infrasonic stations. An atmospheric dust cloud was observed the next morning before sunrise. After careful calibration, the video records were used to compute the bolide trajectory and velocity. The meteoroid, of estimated mass of 3500 kg, entered the atmosphere with a velocity of 15 km s^{-1} on a trajectory with a slope of 60° to the horizontal. The largest fragment ceased to be visible at a height of 17 km, where it was decelerated to 4.5 km s^{-1}. A maximum brightness of absolute stellar magnitude about −18 was reached at a height of 36 km. We developed a detailed model of meteoroid atmospheric fragmentation to fit the observed light curve and deceleration. We found that Košice was a weak meteoroid, which started to fragment under the dynamic pressure of only 0.1 MPa and fragmented heavily under 1 MPa. In total, 78 meteorites were recovered in the predicted fall area during official searches. Other meteorites were found by private collectors. Known meteorite masses ranged from 0.56 g to 2.37 kg. The meteorites were classified as ordinary chondrites of type H5 and shock stage S3. The heliocentric orbit had a relatively large semimajor axis of 2.7 AU and aphelion distance of 4.5 ± 0.5 AU. Backward numerical integration of the preimpact orbit indicates possible large variations of the orbital elements in the past due to resonances with Jupiter.

INTRODUCTION

A wealth of information can be obtained from the laboratory analyses of meteorites. Special value is added if the meteorite fall, i.e., the corresponding bolide, was observed instrumentally. This is because bolide observations provide heliocentric orbits and can place meteorites into their spatial context within the solar system. At the same time, bolide measurements document the atmospheric behavior of incoming meteoroids, providing information on meteoroid bulk properties, which may differ from the properties of recovered meteorites as meteorites represent the strongest parts of the meteoroid.

Until recently, there were only a handful of meteorites with associated instrumental records of their

fall. That number has grown rapidly in the recent years, totaling approximately 15 as of 2011 (for detailed descriptions of some recent cases, see Brown et al. 2011; Spurný et al. 2010, 2012). This is in contrast with tens of thousands of cataloged meteorite finds. A recent compilation and analysis of instrumentally observed meteorite falls can be found in Popova et al. (2011). In particular, that study provides a critical evaluation of the bulk strength of incoming meteoroids and shows that the strength is usually much lower than the strength of recovered meteorites, although there are big variations on a case-by-case basis.

In this paper, we present another piece to the growing mosaic of meteorites with known preimpact orbits. On February 28, 2010, a huge bolide appeared over eastern Slovakia. Although the European Fireball Network (EN) and Slovak Video Network cover this country, bad weather prevented direct imaging of the bolide by dedicated meteor cameras. Fortunately, three surveillance video cameras in Hungary recorded, at least partly, the event. These records allowed us to reconstruct the trajectory of the bolide and recover meteorites. In addition, the bolide light curve was recorded by several EN camera radiometers and seismic stations in the region registered the sonic booms. Infrasonic signatures of the bolide were found at several distant stations, at ranges up to 4000 km. The meteorites were classified as ordinary chondrites of type H5. The bolide data and the number of recovered meteorites show strong evidence for severe atmospheric fragmentation of the meteoroid.

In the next section, we will describe the sequence of all events related to this bolide including meteorite recoveries. We then describe the meteorite properties, followed by details of the bolide trajectory, velocity, and light curve. Next, a model of meteoroid atmospheric flight and fragmentation based on the available data is presented. Finally, we provide the heliocentric orbit of the meteoroid and discuss its possible orbital history.

OVERVIEW OF DATA, THEIR ANALYSIS, AND SEARCHES FOR METEORITES

The evening of February 28, 2010, was cloudy and rainy in most of central Europe. There were clear skies only in the westernmost part of the Czech Republic and around the southern part of German-Polish border. Slovakia and the surrounding areas were completely cloudy except for some cloud gaps in central Hungary. It was raining in Slovakia and the eastern part of the Czech Republic. Despite these unfavorable conditions, hundreds of people in Eastern Slovakia and Hungary noticed an intense flash illuminating the countryside at about 23:25 local time (22:25 UT). Even people inside their homes and watching TV reported the flash. At some places, witnesses reported a cannon-like burst or series of low frequency blasts a couple of minutes after the fireball.

Fig. 1. The atmospheric dust cloud photographed on the morning of March 1 (7 h after the bolide). The upper photo was taken by Dušan Veverka in Brno, the lower photo was taken by Michael Kročil in Dukovany at 6:15 local time. Source: http://ukazy.astro.cz.

The next morning, on March 1, the skies were clear in the eastern part of the Czech Republic. Several people and several web cameras of the Czech Hydrometeorological Institute located at widely separated sites photographed an unusual elongated bluish cloud with fine structure (Fig. 1). The cloud was visible in the eastern sky before sunrise and moved from East to West, in the opposite direction of low-lying clouds. It was photographed from sites as far west as Prague-Libuš and Schlägl, upper Austria (http://home.eduhi.at/member/nature/). These observations occurred some 7 h after the fireball.

There was no doubt that a very bright bolide occurred over Slovakia or Hungary that night. There was a full Moon on February 28 and the bolide was evidently much brighter than the full Moon. We received only one direct sighting of the bolide. Michal Bareš saw the beginning of the bolide low above the

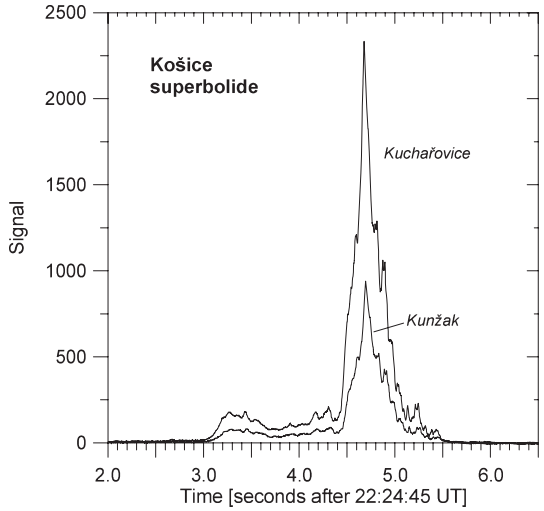

Fig. 2. The radiometric light curves of the brightest part of the Košice bolide from two independent stations, Kuchařovice (16.086 E, 48.881 N) and Kunžak (15.201 E, 49.108 N). The instrumental signal is given in linear scale.

eastern horizon from the city of Plzeň (Pilsen). The bolide disappeared behind clouds and the main flare was seen only indirectly as a cloud illumination.

The Czech and Slovak Republics are covered by the autonomous cameras of the European Fireball Network (Spurný et al. 2007). In Slovakia, cameras of the Slovak Video Meteor Network (Tóth et al. 2011) are also present. From all these cameras, only the camera at Růžová, located in the northwestern part of the Czech Republic, had sufficiently clear skies and was exposing at the time of the bolide. Still, the majority of the bolide was hidden behind clouds close to the horizon. Moreover, the horizon was partly obscured by trees. In any case, the camera did not image the bolide.

The fireball cameras are also equipped with radiometers measuring continuously the total brightness of the sky with a sampling frequency of 500 Hz. Radiometers provide detailed light curves and precise timings of bolides. They are in operation even under cloudy skies, provided that there is no rain or snow. Seven EN cameras recorded the bolide light curve. The two best records are shown in Fig. 2. The Kuchařovice camera was located about 350 km from the bolide. Unfortunately, it was rainy at stations closer to the bolide.

The bolide attracted wide attention of people and the news media in both Hungary and Slovakia. Several video records from surveillance cameras appeared on the Internet showing strong illumination of streets or parking lots caused by the bolide. Fortunately, within a few days (on March 1 and 3, respectively), two video records from Hungary showing part of the bolide became available. The first video was taken in Örkény.

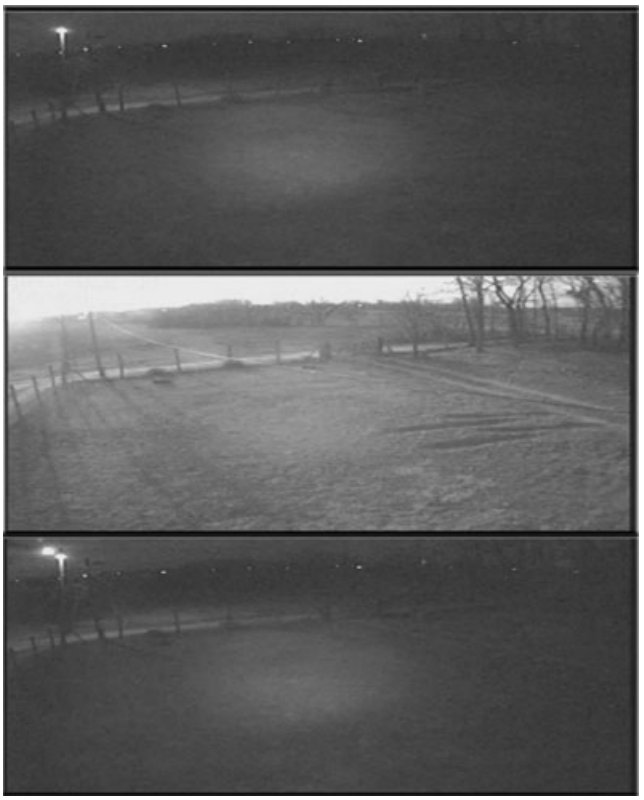

Fig. 3. Three frames from the Örkény video record. The top image shows the scene just before the bolide. The middle frame shows the maximum illumination due to the bolide. The bottom image shows the first frame where the bolide position could be measured, close to the street lamp on the upper left. The lamp was located about 30 m from the camera. In the following frames, the bolide faded and disappeared to the lower left of the lamp. Note that the vertical scale of the images was compressed by a factor of two by the recording software.

At the beginning, only the illumination of the countryside was visible. The bolide then entered the camera field of view and its final luminous stage could be seen close to the horizon (Fig. 3). In addition to the main body, one fragment lagging behind the main body could be measured on two frames. The second video was taken in Telki. The bolide appeared from behind the clouds. After a series of impressive flares, the fading bolide disappeared behind a hill (Fig. 4). Both videos recorded at five frames per second.

One of us (AI) visited the sites on March 5 and 6. The video records were copied from the owners and high-resolution nighttime calibration images were taken from close to the positions of the video cameras by a Canon DSLR camera. The calibration images contained the same terrestrial objects (lamps, buildings, trees) as the video records and a large number of stars in the sky. The videos with the bolide contained no stars. The stars on the

Fig. 4. Four frames from the Telki video record. At the beginning, the bolide was behind the cloud and only illuminated cloud edge can be seen. The third image (bottom left) shows the bolide at maximum light. Before fading out completely, the bolide disappeared behind the horizon. The nearest street lamp was located about 25 m from the camera.

calibration images were therefore used to obtain the angular coordinates (azimuths, zenith distances) of terrestrial objects. The angular coordinates of the bolide were determined from the videos using the terrestrial objects. As an alternative approach, we also tried to measure the GPS coordinates of the foreground terrestrial objects. However, as most objects were relatively close to the camera, this approach did not provide angular coordinates with the required precision (<0.1°).

Later it was learned that a third video of the bolide also exists. It was taken from Budapest. The owner does not want to publish the coordinates and images of his property. We were able to take the calibration images on May 14. This video contains the largest part of the bolide from all three videos and has the best temporal resolution (12.5 frames per second). On the other hand, the bolide, except at the very end of its luminous flight, was heavily saturated in this recording. The position of the bolide could be measured only using dark artifacts inside of the saturated image (Fig. 5).

Table 1 contains the basic data on the videos. In all cases, the field of view was approximately 65 × 50°.

In addition, six seismic stations in the region detected the bolide. The list of the stations is given in Table 2. As usual, the bolide seismic signal was produced by sonic waves propagating through the atmosphere toward the stations. Unlike the previous cases of Morávka and Jesenice (Borovička and Kalenda 2003; Spurný et al. 2010), most of the seismic signal did not contain clearly separated maxima from various meteoroid fragmentation events, which could be used to locate several points along the trajectory. One such prominent event is present in the record of the closest station CRVS at about 22:26:55 UT (see Fig. 6, point 3), but it was identified only at the station KOLS, which lies in the same direction as CRVS. Only a broad maximum, similar to those at CRVS between 22:27:20 and 22:28:00 UT, can be seen at other stations. As the acoustic signal propagated in all directions from the bolide, we interpret this signal as being caused by a series of point-like fragmentations producing spherical waves rather than a cylindrical shock wave propagating perpendicularly to the trajectory. The timing of the signal at various stations enabled us to locate the region in the atmosphere, where the last big fragmentation occurred (i.e., just one "seismic point").

The location of seismic, radiometric, and video stations, which detected the Košice bolide, is presented

Fig. 5. Four partial frames from the Budapest video record. The bottom half of the images were removed to respect the wish of the author of the video. The top image shows the bolide entering the field of view above the nearest lamp. The second image was taken during the maximum light. At the third image, the camera gain was lowered by the automatics (compare the images of lamps). The final image shows the fading bolide split into fragments above the horizon. Above the fragments, meteor train is shining at the position of an earlier flare. The nearest street lamp was located about 20 m from the camera.

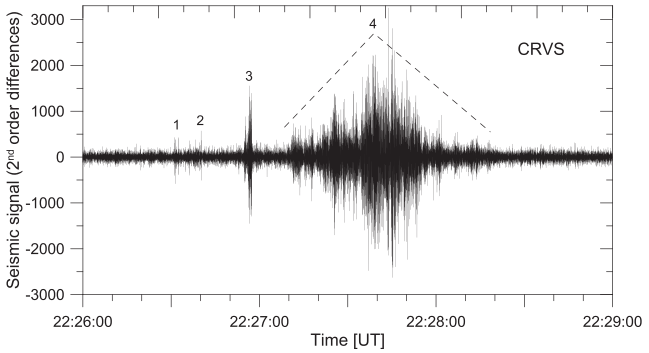

Fig. 6. Seismic record from station CRVS (Z-component). Data were sampled with the frequency of 100 Hz. To enhance the high frequency content, accelerations computed from point to point are shown. The first three distinct signal arrivals are marked by numbers 1–3, while the main, very broad signal is marked by 4. All marked signals are well above the noise level, as confirmed by comparing to more than 10 min of the record around the time of the bolide.

in Fig. 7. Initially, it was not clear whether the bolide occurred over Slovakia or Hungary. The first preliminary reduction (by JB) of the two video records was finished on March 11. It revealed that the bolide flew over the territory of Slovakia, on a steep trajectory, nearly from the West to the East. The last visible fragment terminated its light a few kilometers west from the village of Vyšný Klátov, at a height of about 17 km. The meteorite fall was restricted to the region between Vyšný Klátov and Kavečany, an area of about 6×3 km size. The analysis of seismic data, finished a few days later (by PK), confirmed this general picture.

In between, on March 12, 2010, JT and LK visited a number of villages in the region and interviewed about 30 witnesses. These interviews showed that everybody who was up at the time of the bolide saw a very bright light from inside the house and heard noise like thunder or an airplane. One man from Šaca (13 km SSW from Vyšný Klátov) saw the light, opened the window, and heard a thunder-like noise about 15–20 s after the light. The noise consisted of 4 discrete events like drum beats. After the first one, there was a pause of about 2–3 s, then three beats 1 s each, and finally a cannonade.

There were no reports of direct meteorite hits or accidental finds. The area was covered by fresh snow at that time and was not suitable for searches (the ground was mostly without snow on February 28, 2010 although some remnants of snow were probably present at that time). The first search was organized on March 20, 2010, after most of the snow melted again. Two teams (led by JS and JT, respectively) of 13 people in total started their search on a meadow near Vyšný Klátov. The first meteorite, 27 g of mass (Fig. 8), was found by JT after only 45 min of searching by the second team. Altogether, 13 meteorites were found in two days. Other searches were organized the next week with the participation of Czech and Hungarian colleagues. The largest meteorite (Fig. 9) was recovered by T. Krejčová on March 25 on small meadow on muddy-grass terrain. As of March 28, 2010, 63 meteorites were recovered with masses ranging from 0.56 g to 2.17 kg. One 3 g sample was analyzed by JH and was classified as an H5 ordinary chondrite. On March 31, a press conference was held in Tatranská Lomnica, where the meteorite recoveries were announced to media. Details of the strewn field were not released. According to Slovak laws, collecting meteorites is allowed only by state or academic institutions from the Slovak Republic. Several further

Table 1. Basic data on the video records of Košice bolide.

No	Site	Owner	Coordinates[a] long. E, lat. N	Frames per second	Frame size (pixels)	No. of measured frames
1	Örkény	Gábor Vass, Daniella Fazzi	19.42, 47.12	5	720 × 288	6
2	Telki	Tamàs Meszlényi	18.82, 47.54	5	720 × 576 (668 × 538)[b]	13
3	Budapest	István Asztalos	19.2, 47.5	12.5	800 × 600	50[c]

[a]Approximate coordinates are given. Full precision coordinates were used for calculations.
[b]Active pixels.
[c]Eight measurements were excluded from calculations.

Table 2. Seismic stations which detected the bolide sonic waves.

Code	Name	Country	Longitude E	Latitude N	Altitude *m*	Time of signal
CRVS	Červenica	Slovakia	21.46139	48.90219	476	22:27:37.9
KOLS	Kolonické sedlo	Slovakia	22.27310	48.93330	460	22:30:29.0
NIE	Niedzica	Poland	20.31311	49.41889	649	22:30:14.3
PSZ	Piszkéstető	Hungary	19.89444	47.91839	940	22:31:43.6
STSH	Stebnická Huta	Slovakia	21.24370	49.41670	534	22:29:37.0
TRPA	Tarpa	Hungary	22.53910	48.13040	113	22:32:18.0

Fig. 7. Schematic map showing the location of various stations that recorded the bolide, and the single visual eye witness. Seismic station KECS was out of operation at the time of the bolide. From the seven European Fireball Network stations, which recorded the bolide radiometrically, only station Růžová (Ruz) had mostly clear skies; nevertheless, the bolide remained hidden behind terrestrial objects and/or clouds close to the horizon.

Fig. 8. The first Košice meteorite (27 g) found close to the village of Vyšný Klátov by Juraj Tóth on March 20, 2010.

searches were organized by the Astronomical Institute of the Slovak Academy of Sciences and the Comenius University Bratislava (the same organizers as previous searches) in April, August, and October, 2010. As a result of these searches, the number of recovered meteorites increased to 77 with a total mass of 4.3 kg. Nevertheless, in 2011 we learned that a number of other meteorites, including a 2.37 kg piece, were found by private collectors from abroad and illegally taken out of Slovakia. One additional search was performed in October 2011 using metal detectors. One 6.5 g meteorite was found. Additional privately found meteorites were reported in 2012.

The strewn field is located only 5 km from the edges of the major Slovakian town Košice but is mostly unpopulated. The 78 meteorites recovered in the official searches and 140 privately found meteorites, for which we received masses and coordinates, occupy an area more than 5 km long and more than 3 km wide. The area consists of ridges and valleys, sometimes with steep slopes. The altitudes range from 300 to 600 m above sea level. About 90% of the strewn field is covered by forest, mostly of beech trees. Most of the remaining part is covered by meadows. Only one small settlement, Alpínka, lies inside the strewn field (the villages Vyšný Klátov and Kavečany are just outside). Alpínka is located in a valley, near the road from Košice to Margecany—the only significant road inside the strewn field. The whole area is used for recreation. There is a golf course near Alpínka and the sport and ski center Jahodná lies just north from the strewn field. An

Fig. 9. Two views of the second largest Košice meteorite (2.17 kg) found close to the Alpínka settlement by Tereza Krejčová on March 25, 2010.

overview map showing the second half of the bolide trajectory and the strewn field is given in Fig. 10. More details about the searches and meteorite recoveries will be available in a future article by Tóth et al. (unpublished data).

After the bolide trajectory was known, we searched for infrasound on seven infrasound arrays within 5000 km range of the bolide operated by the International Monitoring System (Christie and Campus 2010) and were able to confirm detection on four of these arrays listed in Table 3. At the time of the bolide, the wind direction in the stratosphere over Eastern Europe was West to East with a prominent stratospheric jetstream having zonal velocities in excess of 50 m s^{-1} between heights 55–80 km. This greatly enhanced infrasound detection at stations to the east of the fireball while suppressing propagation to the west. Airwave detections were made by examining waveforms from each array and searching for coherent wavetrains with arrival directions and propagation timing consistent with the known location and time of the Košice fall and having the expected frequency content for a bolide signal given the known range to the source.

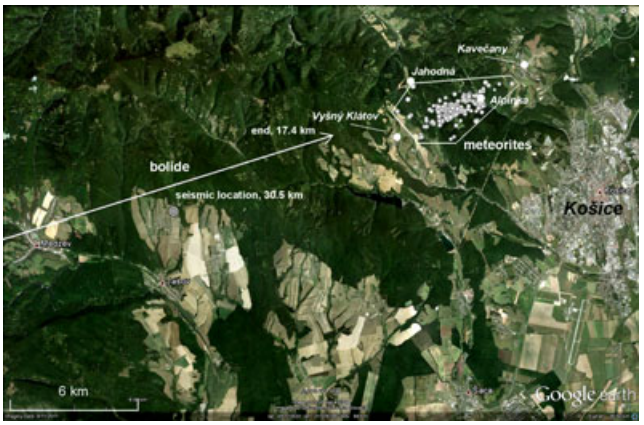

Fig. 10. Map of the surroundings of Košice showing the ground projection of the bolide trajectory determined from the videos, the positions of recovered meteorites, and the independent seismic location of one of bolide explosions (height given in km). Map source: Google Earth.

These detection discriminants are described in more detail in Ens et al. (2012). For each station we analyzed the bolide infrasound signal following the basic bolide infrasound analysis method given by Edwards et al. (2006) as updated and refined in Ens et al. (2012). Table 3 summarizes the signal properties associated with detection of the Košice airwave at each station. These data were used for independent estimation of bolide energy.

METEORITE PROPERTIES

Fusion Crust Coverage

Among the 78 recovered meteorites, 49 are complete individuals covered by fusion crust on the whole surface. The rest have fusion crust coverage ranging from 40 to 95%, where the lowest percentages resulted from hitting rocky terrain or road and the following breakup. The fusion crust is black, rough, and usually about 0.1–0.5 mm thick. The fusion crust has different quality and thickness among individual meteorites, which suggests different ablation history among fragments. Some meteorites have part of their fusion crust very thin and glossier, with the morphology of the coarse meteorite interior still present. This kind of fusion crust may be a result of later fragmentation and gentle ablation phase in the lower atmosphere. The interior of the meteorites is gray. On most meteorites, even those found within one month of the fall, rusty spots are present on the surfaces without fusion crust. The 2.17 kg piece is 70% covered by a primary fusion crust with 20% of the surface covered by a thin glossy, secondary fusion crust while 10% of the surface is free of any fusion crust.

Table 3. Summary of infrasound measurements associated with the Košice bolide[a].

Station	Latitude (deg)	Longitude (deg)	Range (km) (endpoint)	Back azimuth (theoretical) (deg)	Measured Back Azimuth (deg)	Std. Dev. Azimuth (deg)
26	48.84	13.72	540	88.4	88.0	0
31	50.41	58.03	2643	280.4	277.0	1.7
43	56.72	37.22	1397	237.4	235.4	2.1
46	53.95	84.82	4312	289.3	282.1	2.2

Station	Celerity (km s^{-1})	Arrival time (hh:mm:ss)	Total duration (s)	UKMO Wind velocity (m/s)	Maximum Amplitude (Pa)	Period at maximum amplitude (s)
26	0.23	23:04:55	25	−50.47	0.29	2.36
31	0.29	0:54:20	841	54.87	0.24	3.35
43	0.31	23:39:53	488	30.48	0.13	3.45
46	0.29	2:29:28	794	51.74	0.12	3.47

Station	Doppler–corrected Period (s)	Yield (kT)[b]	Fundamental frequency (Hz)	Period @ Fundamenal Frequency (s)	Total signal energy (Pa2)	Integr. Signal-to-noise ratio
26	2.79	0.15	0.35	2.86	0.13	3.26
31	2.87	0.17	0.27	3.70	0.86	15.3
43	3.16	0.24	0.26	3.85	0.43	8.64
46	3.00	0.19	0.22	4.55	0.31	3.58

[a]The measurement methodology applied to each station is outlined in Edwards et al. (2006) and Ens et al. (2012).
[b]From Ens et al. (2012).

Petrography, Texture, Mineral Chemistry, and Classification

One polished thin section (21 × 13 mm) was prepared from meteorite piece no. 15 (3 g). Textural and mineralogical characteristics were studied using a LEICA DMLP petrographic microscope. Mineral compositions were determined using quantitative X-ray wavelength dispersive spectral analysis on a MICROSPEC 3PC Wavelength dispersive X-ray spectroscopy (WDS) system on a CamScan 3200 scanning electron microscope (SEM) at the Czech Geological Survey. The analyses were performed using an accelerating voltage of 15 kV, 20 nA beam current, 1 μm beam size, and ZAF correction procedures for silicate minerals. Analysis of metal grains and sulfides were performed by using an accelerating voltage of 20 kV, 24 nA beam current, 1 μm beam size, and ZAF correction procedures. The counting times were 20 or 30 s for all analyzed elements. To avoid Na volatilization during the analysis of glass and plagioclase, the beam size was increased to 5 μm. Combinations of natural and synthetic standards were used for calibration.

The interior of the studied meteorite is fresh light gray with small brownish veins and taints containing products of terrestrial weathering visible on the surface. This is due to slight weathering processes, as the meteorite was found about three weeks after the fall. Moreover, this meteorite fell close to the road and was affected by salt used to melt snow. The meteorite weathering grade is W0. The chondrules, of around 0.5–1.5 mm in size, are barely visible to the naked eye on the fresh surface.

The thin section shows a highly recrystallized fine-grained granular texture. Chondrule texture is commonly indistinct and only parts of the chondrules are clearly visible. These observations indicate a relatively high metamorphic grade for the Košice chondrite.

Olivine grains show sets of planar fractures and obvious undulose extinction. The observed feldspar does not show planar fractures, however, displays also obvious undulose extinction. The features showing the presence of maskelynite domains within feldspar were not found. All these features and the presence of opaque veins of shock melt and melt pockets indicate stage S3 of shock metamorphism and shock pressures of 15–20 GPa (Stöffler et al. 1991).

Olivine forms a substantial part of this meteorite. Individual olivine grains and olivine in chondrules show very homogeneous chemical composition with low variations typically between $Fa_{18.1–21.5}$ with an average value of $Fa_{19.3}$ ($n = 33$). Zoning of individual olivine grains was not observed and this fact reflects a higher stage of thermal metamorphism. The low-Ca pyroxene

composition ranges from $Fs_{16–19.5}$ with an average value of $Fs_{17.2}$ ($n = 33$). The Wo content of low-Ca pyroxenes varies between $Wo_{0.8–1.2}$. The Fa content in olivine obviously matches the Fs content of low-Ca pyroxene for the H-type chondrites. The high-Ca pyroxene grains are usually associated with plagioclase as well as olivine. The composition of high-Ca pyroxenes is very homogeneous, typically ($En_{48}Wo_{46}Fs_{06}$). The plagioclase grains are obviously associated with high-Ca pyroxene grains with average composition of $Ab_{82}An_{12}Or_{06}$. Kamacite and taenite were also analyzed in Košice meteorite. The characteristic Ni content of kamacite is about 4.8 wt% Ni and for taenite varies in wider range of 45–52 wt% Ni. Accessory minerals of this meteorite comprise chromite, chlorapatite, merrillite, troilite, and pentlandite.

In summary, the Košice meteorite shows all the typical mineralogical features of H chondrites with broad recrystallization and homogeneity of mineral chemical composition reflecting the high stage of thermal metamorphism corresponding to the petrographic type 5. Based on these data the Košice meteorite can be classified as type H5.

Meteorites no. 20 (22 g) and no. 58 (6 g) were later selected for detailed mineralogical analyses done by D. Ozdín and P. Uher (unpublished data). The bulk densities of meteorites were measured by Kohout et al. (Forthcoming). The average value is 3420 kg m^{-3}. Elemental abundances were measured by Plavčan et al. (unpublished data).

BOLIDE TRAJECTORY, VELOCITY, AND LIGHT CURVE

In this section we give the final bolide trajectory and velocity, as they were determined from the analysis of the three video records. We also provide the light curve based on the radiometric records.

Trajectory

The bolide trajectory was computed by the least squares method of Borovička (1990) using the data from the three casual video records. The method takes each observed position of the bolide (azimuth and zenith distance) as a line of sight drawn from the observing site toward the fireball path on the plane of the sky and computes the bolide trajectory as the straight line in 3-D space which minimizes the distances to all the lines of sight from all stations. In performing this trajectory solution we made use of all kinds of bolide positions—the positions of the main body, of the fragment visible toward the end of the trajectory and of the train visible for a fraction of second after the bolide flare.

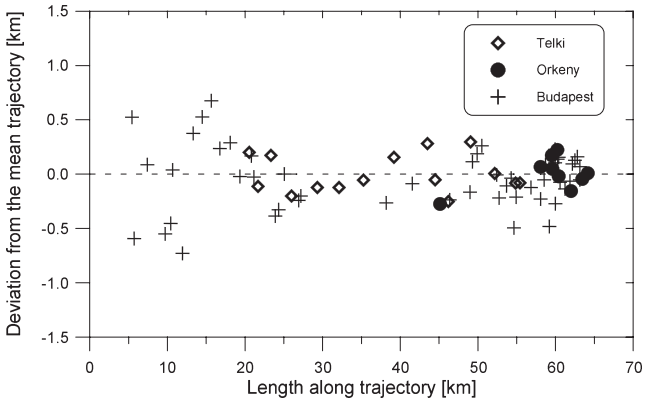

Fig. 11. Deviations of individual positional measurements of the bolide (lines of sight) from the mean bolide trajectory. Data from the three videos are distinguished. The sign of the deviation is positive if the sightline passed above the best-fit trajectory.

The precision suffered from the fact that the calibrations of the videos included some uncertainties due to insufficient number of good terrestrial reference points. Nevertheless, we have several independent checks of the correctness of the trajectory: The positional measurements from the three videos are mutually consistent (i.e., they do not show any large systematic deviations) (see Fig. 11); the velocities derived from individual videos are also consistent; the seismic location of the bolide explosion corresponds, within the errors, with the trajectory from videos; and finally, the trajectory is consistent with the location of meteorites. Still, of course, the precision of Košice bolide trajectory is lower than for bolides observed with dedicated fireball cameras. The precision of the location of the beginning point (i.e., the point where the bolide entered the field of view of the Budapest camera) is about 2 km; for the terminal point it is about 1 km. The uncertainty is generally larger in the SSW–NNE direction, as all three videos saw the bolide nearly in this direction (the maximal convergence angle was 17°, between Telki and Örkény).

The nominal trajectory derived from the videos is given in Table 4. The bolide flew from WSW to ENE on a relatively steep trajectory with a slope of 60° to the horizontal. The radiant azimuth (counted from the north) and zenith distance were $252.6 \pm 4°$ and $30.2 \pm 2°$, respectively. The whole luminous trajectory was over Slovakian territory. The terminal height 17.4 km corresponds to the point where the bolide (the largest fragment) fell below the sensitivity limit of the Örkény camera. At other stations, the bolide crossed the horizon at larger heights (18.3 km in Budapest, 25.0 km in Telki). The first measurement in Telki is at a height of 55.2 km, in Örkény only at 22.7 km, as the

Table 4. Location of Košice bolide trajectory.

	Longitude (deg E)	Latitude (deg N)	Height (km)
First point[a]	20.705 ± 0.011	48.667 ± 0.021	68.3 ± 1.4
Terminal point	21.083 ± 0.005	48.746 ± 0.010	17.4 ± 0.6

[a]Entering the field of Budapest video camera.

bolide was too bright to be measured earlier. The train, however, could be measured at a height of 34 km from Örkény.

The seismic location was computed from the times of arrival of the strongest signal to the seismic stations (see Table 2), using the known time of bolide maximum and the average speed of sound between the heights of approximately 30 km and the ground, as computed from the actual meteorological measurements. The resulting position was corrected for the drift caused by high altitude winds. The correction was 1 km to the west and 0.35 km to the north. The final position is 20.981°E, 48.714°N, $h = 30.5$ km with a precision of ≈2 km. This point lies 1.4 km from the nominal video trajectory. The two solutions are therefore consistent within the postulated errors.

Velocity

The bolide positional measurements on individual video frames projected onto the derived trajectory define the position (length) along the trajectory as a function of time. The length was counted from the first measurement on the Budapest video. The video frame rates (5 Hz for Telki and Örkény, 12.5 Hz for Budapest) define the relative time scale for each video. To take all videos together, the offset of their time scales had to be determined. This was done by minimizing the time differences for a given length. Finally, the relative time was converted to absolute time by adjusting the Budapest light curve to the radiometric light curve (see below). The absolute timing of radiometers is better than 5 ms. The computer time is corrected by the PPS signal from the GPS receiver.

The length as a function of time is given in Fig. 12. It is linear at the beginning, implying constant velocity, as expected for a massive meteoroid high in the atmosphere. The initial velocity, 15.0 ± 0.3 km s^{-1}, was computed from the linear fit of observations until the time 3.2 s. The quoted error includes also uncertainties in geometry and time correlation of the video.

At lower heights, the bolide was clearly decelerated. The velocity at the end decreased to 4.5 km s^{-1}. The form of the deceleration, together with the light curve, was used as the input for modeling of the bolide as described in the next section. At the end of the trajectory, a fragment clearly separated from the main body as recorded on several consecutive frames (Fig. 13) and its position as a function of time was also measured (Fig. 12).

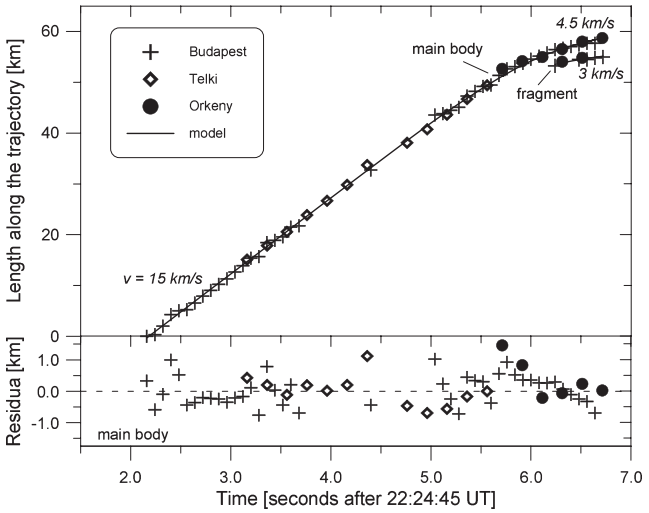

Fig. 12. The observed length along the trajectory as a function of time for the three videos. Data are scarce in the middle of the trajectory, where the bolide was very bright and difficult to measure. The slope of this function gives the bolide velocity. The velocity was 15 km s^{-1} at the beginning and 4.5 km s^{-1} at the end. The fragment visible on several frames near the end of the bolide (see also Fig. 13) was measured as well. It was about 3 km behind the main body and its velocity decreased to 3 km s^{-1}. The bottom panel shows the residuals in length between the observations and the model of the bolide. The observed lengths (and heights) are provided in Data S1 of supporting information.

Light Curve

The bolide light curve was well observed by the radiometers, in relative units, as a function of time (Fig. 2). It was therefore desirable to assign the absolute timing of the radiometers to the relative time scale of the video records to be able to study the brightness of the bolide not only as a function of time but also as a function of height.

To fulfill this task, we performed a relative bolide photometry calibration of the Budapest video. The bolide itself was heavily saturated on the video, so it could not be measured directly. We measured the illumination of parts of the scene. As the bolide brightness varied enormously during the flight, different parts of the scene (sky, landscape) were measured in different bolide phases. Nevertheless, the resulting light curve resembled the radiometric light curve quite well, so there was no problem adjusting the time shift (see Fig. 14).

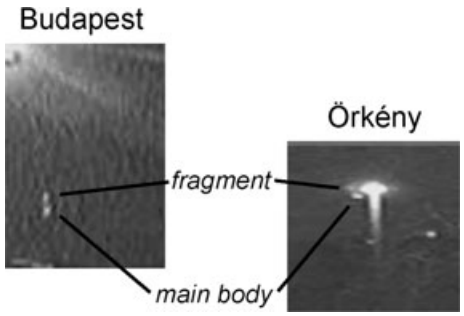

Fig. 13. Part of video frames from Budapest and Örkény clearly showing a fragment separated from the main body in the final stages of the bolide.

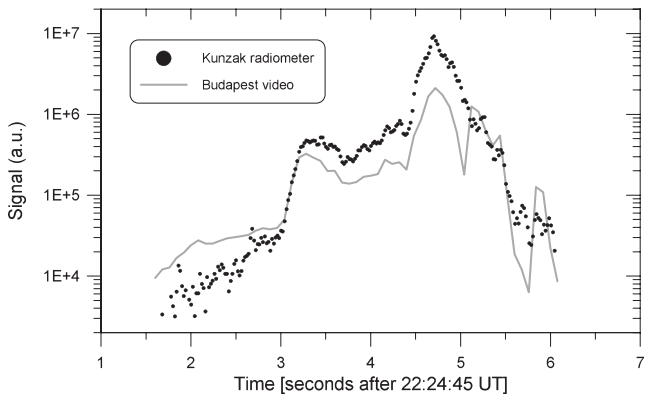

Fig. 14. The rough bolide light curve constructed from the Budapest video was compared with the Kunžak radiometric signal. The vertical scale of both curves was shifted to nearly match (but the video response was nonlinear due to saturation). The time scale of the video was adjusted using the features on the light curve.

The absolute calibration of the signal was done using the Kunžak camera; this is the same camera which recorded the Martin and Jesenice bolides under similar conditions during the full Moon period (see Spurný et al. 2010). Similarly as for Jesenice, the Martin fireball was used for calibration. We computed the range and zenith distance of the bolide as seen from Kunžak as a function of time. The range was between 416–433 km. The zenith distance was between 82.5–89.7° for bolide heights 68–17.5 km. The observed signal was corrected for instrumental response of the radiometer as a function of zenith angle (measured in the laboratory) and for bolide range. Furthermore, we computed the standard atmospheric extinction as a function of zenith distance. As part of the light is always scattered by the upper atmosphere, there is a nonnegligible signal even if the source lies on or below the horizon. This feature could not be exactly calibrated but after some trials we estimated that the signal at the horizon is 0.5% of that in zenith for our system.

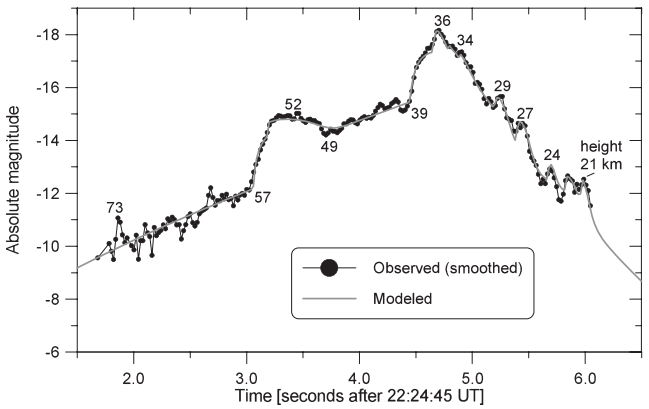

Fig. 15. The calibrated light curve from the Kunžak radiometer and the modeled light curve. The observed light curve was smoothed by averaging 10 consecutive measurements. The height of the bolide in km is given near some of the light curve features. The observed light curve is provided in Data S1.

There is a significant difference between the Martin and Košice bolides in that Martin was detected under clear sky while Košice was detected under a completely cloudy sky in Kunžak. Nevertheless, the radiometer is always adjusted to the same signal level during the night by modifying the high voltage of the photomultiplier. The signal of the bolide is compared with the background signal, which was defined by the full Moon in this case. We therefore decided to ignore the difference between the clear and cloudy night, assuming that the Moon and the bolide were affected in a comparable way.

The resulting calibrated light curve is shown in Fig. 15 together with the modeled light curve (see the next section). The maximum absolute magnitude of −18 was reached at 22:24:49.7 when the bolide was at a height of 36 km. Owing to the extremely difficult calibration of the radiometric signal in this case, the absolute magnitude scale is uncertain by at least one stellar magnitude.

MODEL OF METEOROID ATMOSPHERIC FRAGMENTATION

The observed light curve and deceleration of the bolide was used to estimate the initial mass of the meteoroid and its fragmentation history in the atmosphere. The model also enabled us to restrict the expected masses and locations of fragments reaching the ground and compare them with the actual meteorite recoveries.

The model is based on the fact that meteoroid fragmentation leads to a sudden increase in bolide brightness, because the total meteoroid surface area increases after the fragmentation. A bright flare is

produced if a large number of small fragments or dust particles are released. In contrast to similar modeling we performed for the Jesenice bolide (Spurný et al. 2010), we did not use the schematic shape of the flares but we tried to model the whole light curve more rigorously by setting up the mass distribution of fragments and/or dust particles released at each fragmentation point. The dust particles were allowed to be released either instantaneously or gradually, using the meteoroid erosion concept we originally developed for small meteoroids (Borovička et al. 2007). The ablation and radiation of individual particles were computed independently and the summed light curve then computed.

The model is a trial-and-error fit of the light curve. We tried to reproduce the major features of the light curve by adjusting the times of fragmentation and the numbers and masses of fragments and dust particles. The deceleration at the end of the trajectory was taken into account as well. This approach gives us an idea about the strength and structure of the original meteoroid but surely does not provide an exhaustive description of all existing fragments.

Parameters of the Model

The model is based on the standard single-body theory of meteoroid ablation, deceleration, and radiation. The single-body model was applied to each fragment from its birth in the fragmentation of its parent fragment to its own subsequent fragmentation or until the velocity decreased below the ablation limit (set at 2.5 km s^{-1}). The equations of the single-body theory are given in Ceplecha et al. (1998, pp. 348–350). The initial values for each fragment are the time, height, velocity, slope of the trajectory, mass, ablation coefficient, and shape-density coefficient (combination of drag coefficient, shape coefficient, and bulk density). The integral solution of the single-body theory we used required that the ablation coefficient and shape-density coefficient were kept constant for the entire flight of any fragment. We assumed that all fragments follow the same trajectory given in Table 4, with the slope of 60° to the horizontal. The trajectory was assumed to be straight but the Earth curvature was taken into account. Atmospheric densities were taken from the CIRA72 atmospheric model. To reduce the number of free parameters we used the same ablation coefficient of 0.005 s^2 km^{-2} and the same bulk density of 3400 kg m^{-3} for all fragments. The value of bulk density was known from meteorite measurements. The value of the ablation coefficient was chosen in accordance with previous studies of the ablation of fragments between the fragmentation events (Borovička and Kalenda 2003; Ceplecha and ReVelle 2005). The precision of the deceleration measurements was not sufficient for an independent computation of the ablation coefficient. The value of ΓA (drag coefficient times the shape coefficient) was set to 1.0 for the initial meteoroid high in the atmosphere, 0.8 for fragments born at medium heights (60–30 km), and 0.7 for fragments born at lower height to account for the decreasing drag in the denser atmosphere due to the formation of a protective layer of compressed air in front of the fragments. This decrease was also discussed by Borovička and Kalenda (2003).

For computing the light curve, the value of the differential luminous efficiency, τ, i.e., the fraction of instantaneous loss of meteoroid kinetic energy (due to both deceleration and mass loss) converted into radiation, must be given. Luminous efficiency is a poorly known quantity depending on meteoroid velocity, mass, and perhaps on other quantities. We assumed that τ is directly proportional to velocity. As for mass dependency, ReVelle and Ceplecha (2001) found that there is a steep increase in τ at masses of about 1 kg. The typical luminous efficiency for large stony bodies (type I bolides) was found to be about 5%. For small bodies (gram masses) it was up to 10 times lower. We assumed τ to approach 5% for very large masses (approximately 1000 kg) at velocity of 15 km s^{-1}. The lower limit of τ was important when modeling radiation of small fragments and dust particles. We were unable to fit the observed flares with very low values of τ. We had to set the lower limit at 2.5%. It is possible that values of τ smaller than 1% are applicable for small meteoroids high in the atmosphere but larger values are valid for the same masses at lower heights, when they separate from larger bodies.

Following ReVelle and Ceplecha (2001) we used natural logarithm and hyperbolic tangent functions to compute τ:

$$\ln\tau = -1.45 + \ln v + 0.35\tanh(0.38\ln m), \qquad (1)$$

where v is velocity in km s^{-1} and m is mass in kg; τ is in percent of kinetic energy loss. In converting radiated energy into meteor magnitudes we used the zero-visual-magnitude meteor energy of 1500 watts, valid for the usual vapor temperature of 4500 K (Ceplecha et al. 1998, p. 365). At 15 km s^{-1}, τ is 2.5% for 1 g or less, 2.75% for 100 g, 3.5% for 1 kg, 4.5% for 10 kg, and 5% for 1000 kg or more.

Our mass-dependence term is very similar to that of Ceplecha and ReVelle (2005); nevertheless, the absolute values of the intrinsic luminous efficiency coefficient introduced by Ceplecha and ReVelle (2005) are about 3–4 times smaller than in ReVelle and Ceplecha (2001) and do not exceed 1.5% for approximately 100 kg

bodies. Nevertheless, values of τ of about 4% were found by a single-body analysis of the MORP 219 fireball by Gritsevich and Koschny (2011). MORP 219 is the only fireball in their sample of three fireballs with relatively low ablation coefficient, which means it was not significantly affected by fragmentation and hence the single-body analysis may be justified. Note that Ceplecha and ReVelle (2005) assumed that luminous efficiency is also a function of meteor position (relative to maximum light or trail beginning). We did not need such an assumption.

Fragmentation Modes

In our model, fragmentation means that the mass of a meteoroid is suddenly converted into one or more of the following objects:

1. Individual daughter fragments of smaller mass. The mass and physical parameters (ablation coefficient, bulk density, ΓA) of each fragment are specified and the fragments are then followed according to single-body theory.
2. A group of fragments of the same mass and physical parameters. This option is similar to the previous one. Further development is computed only once and the resulting radiation intensity is multiplied by the number of fragments. Of course, this approach is an idealization because in reality not all fragments will be exactly the same. But the complexity of the model and computational demands are reduced this way.
3. Dust, i.e., a large number of small particles. The physical parameters of all particles are assumed to be the same. Their masses may be either the same or there is a mass range specified. The former case is equivalent to the option 2 (group of fragments). The only difference is that the user specifies the total mass of the dust, not the number of fragments. In the latter case, the lower and upper mass limit and mass distribution index are specified. The code then sorts the particles into mass bins (10 bins per order of magnitude of mass) and computes the number of particles in each bin. Further development for each mass is computed once and the output light is multiplied by number of particles in the bin.
4. Eroding fragment or, in other words, a clump of dust. In this case the dust particles are not released and do not start to ablate immediately at the fragmentation point. Instead, they are held together in one fragment at the beginning and then released gradually. To describe this process, the formalism of meteor erosion (Borovička et al. 2007) is used. The fragment is subject not only to ablation, governed by ablation coefficient, σ, but also to erosion, i.e., loss of mass in the form of solid particles, governed by the erosion coefficient, η, which has the same units as σ (s^2 km^{-2} or, equivalently, kg MJ^{-1}) but is larger. At each time step, the mass of released dust and the number of particles in each mass bin are computed. The procedure is repeated until the fragment is eroded away completely. The ablation and radiation are then computed for each mass bin and for each time of release.

The initial height and velocity of each fragment or dust particle are given by the height and velocity of their parent fragment at the moment of release. The summary mass of all daughter fragments and the dust is equal to the mass of the parent fragment. In practice, the masses of fragments and eroding fragments are specified and the rest is assumed to be released as a dust. The release of dust causes a steep increase in bolide brightness (appearing as a step on the light curve), followed immediately by a decline (if the particles are small). The separation into a large number of macroscopic fragments causes a smaller step, after which the prefragmentation slope of the light curve is resumed. The formation of an eroding fragment leads to a gradual increase in brightness followed by a gradual decrease, i.e., a smooth flare (a hump) on the light curve is produced. The shape and duration of the flare depends on the erosion coefficient and on the masses of the dust particles. The formalism of erosion can be used also for relatively large fragments released gradually.

The appropriate fragmentation times and the involved fragmentation modes were selected according to the shape of the light curve. The parameters of the fragments and the dust were then tuned to reproduce the observed light curve as well as possible. We used a time step of 0.02 s. The mass of the largest fragment was also restricted by the observed deceleration of the bolide.

Application to Košice

The full details of our best solution are given in Table 5. Of course, we do not claim that it is a unique solution. The fragmentation heights have been determined well. The masses of the fragments are rough and should be correct within an order of magnitude. Although the number of fragments involved in the model is relatively large, still it is an idealization and the reality was surely more complex. Nevertheless, the general behavior described in the following paragraphs should be correct.

The initial mass of the meteoroid was estimated to be 3500 kg (corresponding to a diameter of 1.25 m). Owing to the uncertainties in absolute photometry and

Table 5. Parameters of the modeled Košice fragmentations.

Fragmentation			Parent fragment		Daughter fragments and dust				Dust	Meteorites[c]
Time[a] (s)	Height (km)	Dyn. Pres. (MPa)	Name	Mass (kg)	Type[b]	Name	Total mass (kg)	Erosion coeff. (s^2 km^{-2})	Masses (kg)	Mass (kg)
3.06	56.8	0.09	MAIN	3496	F	1	3345			
					EF	2	150	2.5	10^{-6}	
					D	DM	1		10^{-6}	
3.20	55.0	0.11	1	3344	F	11	2030			
					GF	12	120 × 5			
					GF	13	30 × 10			
					GF	14	40 × 10			
					D	D1	14		2×10^{-5}	
4.46	38.7	0.97	11	2009	F	111	100			
					F	112	50			
					F	113	20			
					EF	114	1740	0.7	$0.01–10^{-4}$	≤ 0.006
					D	D11	99		0.01	≤ 0.006
4.66	36.6	1.13	12	4.5 × 120	EF	121	4	0.5	10^{-5}	
					D	D12	0.5		10^{-5}	
4.80	34.8	1.47	13	9.0 × 30	EF	131	7	0.3	10^{-4}	
					D	D13	2		10^{-4}	
4.90	33.7	1.70	14	8.9 × 40	EF	141	8	0.1	10^{-4}	
					D	D14	0.9		10^{-4}	
5.22	29.3	3.6	111	91.7	F	1111	30			
					EF	1112	60	0.3	$0.01–10^{-4}$	≤ 0.008
					D	D111	1.7		10^{-4}	
5.38	27.6	4.0	112	43	F	1121	0.5			0.34
					EF	1122	40	0.3	$0.01–10^{-4}$	≤ 0.008
					D	D112	2.5		10^{-4}	
5.68	24.2	5.6	1111	26.1	F	A1	20			
					EF	A2	5.5	0.3	$0.1–10^{-4}$	≤ 0.08
					D	DA	0.6		10^{-4}	
5.82	23.6	4.4	113	14.6	EF	1131	14.4	0.2	$0.2–10^{-4}$	≤ 0.17
					D	D113	0.2		10^{-4}	
5.96	21.6	5.9	A1	18.1	F	A11	8			6.5
					F	A12	2.4			2.0
					EF	A13	7.7	0.3	$0.3–10^{-4}$	≤ 0.3

[a]Seconds after 22:24:45 UT.
[b]F—fragment, GF—group of fragments, EF—eroding fragment, D—dust.
[c]Masses of meteorites larger than 1 g reaching the ground.

luminous efficiency, there is an uncertainty in the mass of a factor of 3.

The first significant fragmentation, probably in two phases, occurred at heights of 57–55 km. About 1500 kg from the original mass was separated from the meteoroid. A smaller part of it, 165 kg in our model, was released as dust particles of masses 10^{-5} to 10^{-6} kg (i.e., millimeter-sized). Most of these fragments were not released suddenly but were gradually eroded away. Their evaporation formed a hump on the light curve at heights 57–49 km. A larger mass was released in the form of about 200 macroscopic fragments of masses 5–10 kg (approximately 15 cm size). The presence of these fragments was responsible for the elevated brightness of the bolide between 49–39 km in comparison with the trend from above 57 km.

The major fragmentation of the main body, which was still about 2000 kg in total mass, occurred at the height of 39 km. Only a few (probably three) large compact fragments of masses 20–100 kg survived this disruption. We will call them survivor fragments. The mass of about 100 kg for the largest one was derived from the deceleration of the bolide. All of them fragmented again at lower heights below 30 km, producing minor flares on the light curve.

The majority of the mass released at 39 km (1740 kg in our model) was converted into a clump of small fragments of masses of 10^{-2} to 10^{-4} kg, which

were gradually separated over the interval of heights of 39–32 km. They caused the broad maximum of the light curve. It is also possible that up to 100 kg of mass was released immediately at 39 km in the form of small (10^{-2} kg) fragments, but data are insufficient to restrict their amount.

All 5–10 kg fragments formed at 55 km were destroyed at heights 36.5–34 km and converted completely into "particles" of 10^{-4} to 10^{-5} kg. Minor flares caused by these fragmentations are superimposed with the broad bolide maximum. In particular, the absolute peak at 36 km was formed.

The three survivor fragments were the only bodies larger than 1 kg that managed to reach heights below 30 km. Their subsequent history is restricted not only by the light curve but also by the deceleration data and images of the final phase of the bolide. There was a significant gap between the main body and the second fragment (see Figs. 12 and 13). This fact could be reproduced only if the second fragment was formed at the flare at 27 km and was relatively small (≤ 0.5 kg). At the same time, a relatively large mass ($\approx$20 kg) was required to continue down to the height of 21.5 km, where the final fragmentation occurred. The deceleration after the flare at 21 km is consistent with a remaining mass of 2–8 kg. It is, nevertheless, possible that two or more fragments in that mass range were present. Our conclusion is that the observed main body was formed at the end by one or more fragments in the mass range 2–8 kg and of total mass no more than 10 kg. Pieces smaller than 0.3 kg could be formed in the fragmentation at 21.5 km as well but they did not contribute significantly to the bolide luminosity after 6.2 s.

The overall scheme of the fragmentation model is presented in Fig. 16. The numerical values are given in Table 5. In all cases we used ablation coefficient $\sigma = 0.005$ s^2 km^{-2}, mass distribution index $s = 2$, and ΓA from 1.0 to 0.7 depending on fragment formation height.

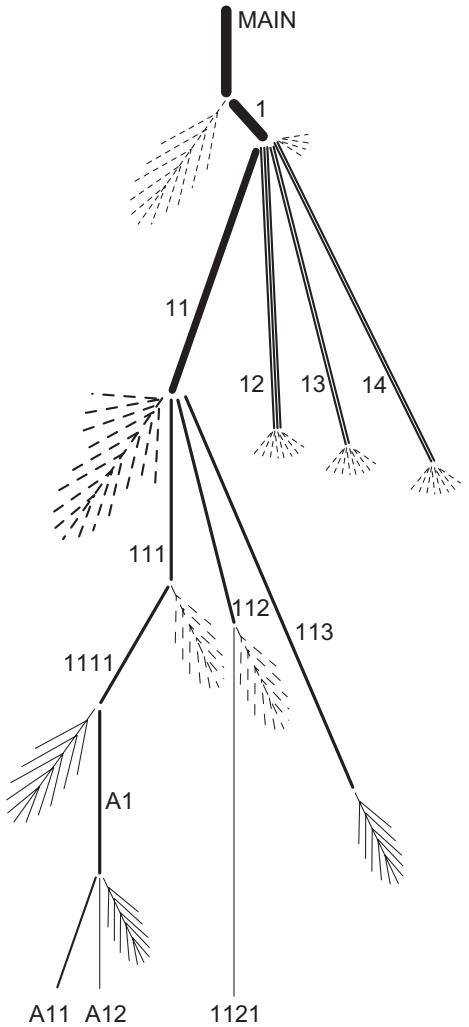

Fig. 16. Schematic of the Košice fragmentation model. Individual fragments and groups of fragments are designed by their names (numbers). The widths of the lines are proportional to fragment masses. Eroding fragments and dust releases are drawn schematically. Dotted lines are used if only small particles were released; dashed lines mark presence of medium-sized fragments; solid lines are used if sizable fragments (≥ 0.1 kg) were produced as well.

Discussion of Model Parameters

As we used a priori assumed values of the ablation coefficient, drag coefficient, and luminous efficiency, we investigated how the model results would change if different values were chosen.

A larger ablation coefficient, e.g., 0.015 s^2 km^{-2} instead of 0.005 s^2 km^{-2}, would produce higher mass loss and therefore higher luminosity at the beginning of the bolide. To compensate for this effect, we would need to lower the initial mass and the luminous efficiency for large bodies. Moreover, with lower mass available, we would need to increase the luminous efficiency for small fragments (dust) to be able to explain the amplitude of the flares. A reasonable fit was obtained with the initial mass of 3000 kg (instead of 3500 kg) and the range of luminous efficiency at 15 km s^{-1} from 3 to 3.5% (instead of 2.5–5%).

A lower ablation coefficient, e.g., 0.002 s^2 km^{-2}, would need only small adjustments, namely increasing the initial mass to 4000 kg and the upper limit of luminous efficiency to 5.5%.

The drag coefficient will in reality smoothly decrease with decreasing bolide height. Our numerical approach does not enable us to introduce a smooth change in ΓA, so we assumed $\Gamma A = 1$ at the beginning

and $\Gamma A = 0.7$ for fragments created at low heights. Assuming $\Gamma A = 0.7$ for the whole trajectory would require an increase in the initial mass to 4500 kg to explain the luminosity at the beginning. With more mass available, we would also have to lower the luminous efficiency for the dust to 2.25%. These changes are relatively minor despite the severe change in ΓA at the beginning. Our stepwise approach to ΓA therefore does not negatively influence the results.

Finally, we checked if the data can be fitted with the low values of luminous efficiency given in Ceplecha and ReVelle (2005). We set τ to 0.6–1.4% at 15 km s^{-1}, depending on mass. To explain the observed luminosity, we needed to increase the initial mass to more than 11,000 kg and to use a higher ablation coefficient of 0.010 s^2 km^{-2}. To explain both the deceleration and luminosity in the second half of the trajectory, ΓA was kept 1.0 for the whole trajectory. This solution does not contradict any observation directly and was able to predict meteorites of reasonable masses, but we consider it rather unrealistic because of the high ΓA at the end and very high initial mass (see the comparison with infrasonic data below).

In summary, the low precision of deceleration measurements does not allow us to restrict the value of the ablation coefficient very tightly. In principle it may be anywhere between 0.001 and 0.015 s^2 km^{-2}. The differences in radiative output for different values of σ can be compensated by changing the initial mass and the value of the differential luminous efficiency. The luminous efficiency is therefore also not certain but probably was between 2% and 6% at 15 km s^{-1}. Nevertheless, it is important to note that our main result, the fragmentation positions, is not affected by these uncertainties. Also the resulting masses of meteorites are nearly the same for all combinations of parameters.

Comparison With the Seismic Record at Station CRVS

After the bolide trajectory was computed, the seismic record at the closest station CRVS, which lies in the flight direction with only a small side step of about 10 km, could be compared with our fragmentation analysis based on the light curve. As the coordinates of the bolide (the leading fragment) are known at any time T, the expected arrival time at CRVS of the sonic signal originated at the time T can be computed (taking into account the distance to the station, average speed of sound from that height, and the wind drift). The seismic signal can therefore be assigned to the source height. Direct comparison with the light curve is also possible but we must keep in mind that the light curve was measured as a function of time, not height, so any light produced by fragments other than the leading one has the height assigned incorrectly. But the difference is significant only for some of the flares toward the end of the bolide.

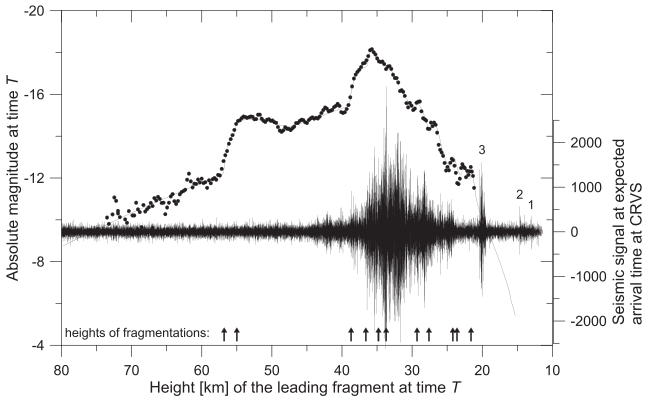

Fig. 17. A comparison of the seismic signal at station CRVS with the fragmentation heights and the light curve. The first three sonic arrivals are marked 1–3 (compare to Fig. 6). See the text for the explanation how this plot was produced.

The comparison is plotted in Fig. 17. In general, we can see that the period of strong seismic signal corresponds quite well with the period of high luminosity of the bolide and the interval where the meteoroid fragmentations were revealed by our analysis. The seismic signal is weaker at higher altitudes but this is understandable for two reasons. First, the distance to the station was larger, so the received signal was weaker due to the inverse square law. Second, the lower density of the atmosphere was less favorable for generating the sonic signal. Nevertheless, a clear sonic signal was produced at least from heights 45 km downwards. Two minor flares on the light curve between 40 and 45 km, which we did not attempt to fit, clearly correspond to seismic signal.

A closer view reveals a small systematic shift between the seismic signal and the light curve/fragmentation points. The seismic signal seems to be generated at somewhat lower heights. The shift is most visible between the last fragmentation point and the distinct seismic signal marked 3 in Fig. 17. We checked the video record and there is no sign of any flare at heights below 21 km, which could be attributed to seismic signal 3. We also checked that the wind drift was correctly taken into account in our computations. Nevertheless, the difference may still be caused by the combined error of both methods (video and seismic). It is possible that a more rigorous approach to computing the sound propagation (e.g., that of Edwards and Hildebrand 2004) would remove the discrepancy. An alternative explanation, although less likely, could be that the blast wave radius (Edwards 2010) of the explosions producing the sound was of the order of 1–2 km, so that the sound was

Table 6. Mass distribution of recovered meteorites compared with model output.

	Recovered meteorites		Model prediction	
Mass range	Number	Total mass (kg)	Number	Total mass (kg)
0.1–1 g	3	0.002	2,000,000	550
1–10 g	100	0.51	200,000	500
10–100 g	96	2.92	240	6.5
0.1–1 kg	17	3.31	12	2.2
1–10 kg	2	4.54	~2	$\leq$ 8.5

effectively generated closer to the station CRVS than was the fragmentation point.

In any case, we can conclude that the sonic waves detected at CRVS (and other stations too) were generated by meteoroid fragmentations producing nearly spherical waves. In contrast, the seismic data of the well-observed Neuschwanstein meteorite fall were interpreted as being caused mainly by cylindrical line source blast wave (ReVelle et al. 2004). This does not mean that cylindrical waves were not produced in the Košice event. The location of the seismic stations relative to the bolide trajectory simply did not allow cylindrical waves to reach the stations. On the other hand, atmospheric fragmentation was more complex and severe in Košice than in Neuschwanstein. It is also remarkable that the sonic energy generated along the trajectory in the form of spherical waves had a very similar pattern to the radiative output. It is clear that the same process, namely meteoroid fragmentation and subsequent deceleration and ablation of dust and small fragments, produced both the light and the sound. We can also say that the seismic data confirmed our fragmentation analysis.

The weak but distinct sonic arrivals 1 and 2 (see Figs. 6 and 17) originated at heights below 17.4 km where the bolide ceased to be visible. We interpret the signal 1, from a height of about 13 km, as corresponding to the point where the speed of the largest fragment dropped below the speed of sound. At that point the cylindrical waves became spherical and seismic energy accumulated. Signal 2, from approximately 15 km, may be sound speed crossing of another fragment or a late fragmentation not detected in light.

Comparison with Meteorite Mass Distribution

The model provided the masses, heights, and decelerations of all modeled fragments at the moment when their velocity decreased to 2.5 km s^{-1} and their ablation stopped. The mass distribution of the modeled fragments is compared with the mass distribution of the recovered meteorites in Table 6.

The model predicts a gap of total mass for meteorites in the 0.1–1 kg range. This gap seems to be really observed, as the total recovered mass in the 0.1–1 kg range is only slightly larger than in the 0.01–0.1 kg range, although the recovery efficiency must be clearly better for larger masses. On the other hand, with new meteorites reported, the total number of meteorites larger than 0.1 kg already exceeds the model predictions. As many of the fragments are outliers in the strewn field, we suspect that they may be fragments formed at high altitudes (>30 km), which were not considered in the model.

The meteorite recoveries at low masses are, of course, incomplete. The model predicts huge numbers of meteorites smaller than 10 g, from which only a tiny part was recovered. Note, however, that the modeled numbers should be taken as upper limits, as part of the fragments may have been additionally fragmented in the atmosphere. It must be also noted that the bolide light curve provided only little hints about the number and masses of small fragments. The flares could be fitted with different combinations of fragment mass range, their mass distribution index, and the erosion coefficient.

Comparison with Meteorite Strewn Field

We can compare not only the mass distribution but also the actual positions of meteorites on ground to the model. The predicted meteorite positions were computed by the dark flight code of Ceplecha (1987). The input is the position, velocity, and deceleration of each fragment at the moment of ablation stop (assumed to be at velocity 2.5 km s^{-1}—this assumption is not crucial as the ablation coefficient was very small) and the high altitude wind field. We assumed all fragments to follow the same trajectory during the ablation phase. In reality, the fragments gain some lateral velocity during the fragmentation process (e.g., Borovička and Kalenda 2003), which leads to larger dispersion in the strewn field. Nevertheless, we found the effect to be relatively small in our case (approximately 100 m) for lateral velocities up to 0.1 km s^{-1}.

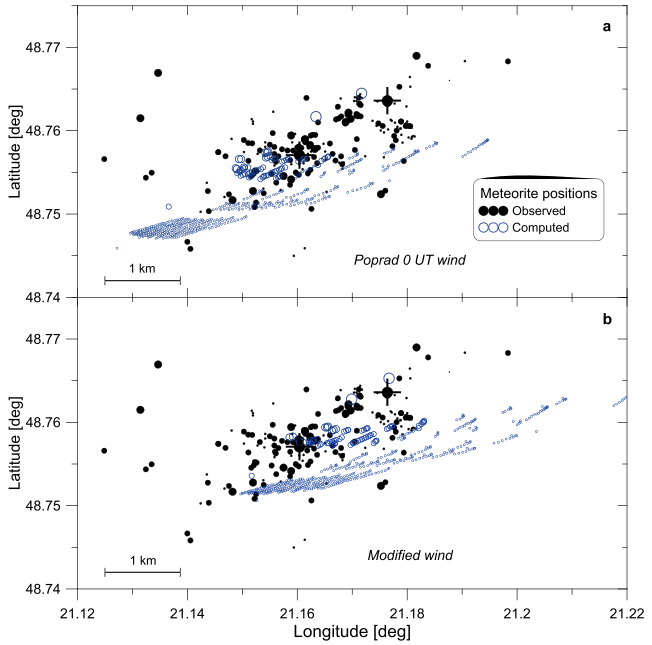

Fig. 18. Comparison of the positions of recovered meteorites with the modeled meteorite positions using the Poprad radiosonde wind (top) and manually modified wind profile (bottom). The wind profiles are shown in Fig. 19. The sizes of the symbols correspond to the meteorite masses (one symbol size per order of magnitude mass). The two largest meteorites are emphasized by crosses. The modeled meteorite sample contains only representative pieces, not all expected meteorites.

The comparison of the actual and predicted strewn field is presented in Fig. 18. The observed strewn field was notable in that there was no evident mass sorting. Meteorites of different masses were well mixed. The only exception is that the western end of the strewn field contained only meteorites of medium masses, not very small ones (despite favorable search conditions) or large ones. Such behavior can be well explained by the high altitude winds.

The wind profiles obtained from two sources are given in Fig. 19. We preferred the profile measured by the radiosonde launched in Poprad (70 km WNW from the strewn filed) at 0 UT. The UK Met Office global model provided data for 640 × 480 global grid once per day at 12 UT (Met Office et al. 2006). The nearest data point was located 20 km south from the bolide end point. All data agreed that the strongest winds of about 40 m s^{-1} were encountered at the heights of about 10 km and were flowing from WSW to W directions. Above 25 km, the winds were generally from the east with a speed of about 10 m s^{-1}. The Poprad data showed a dip in wind speed and rapidly changing wind direction at heights 0–5 km. This feature is not present in the global model. We may speculate that it was caused by the proximity of the High Tatra mountains

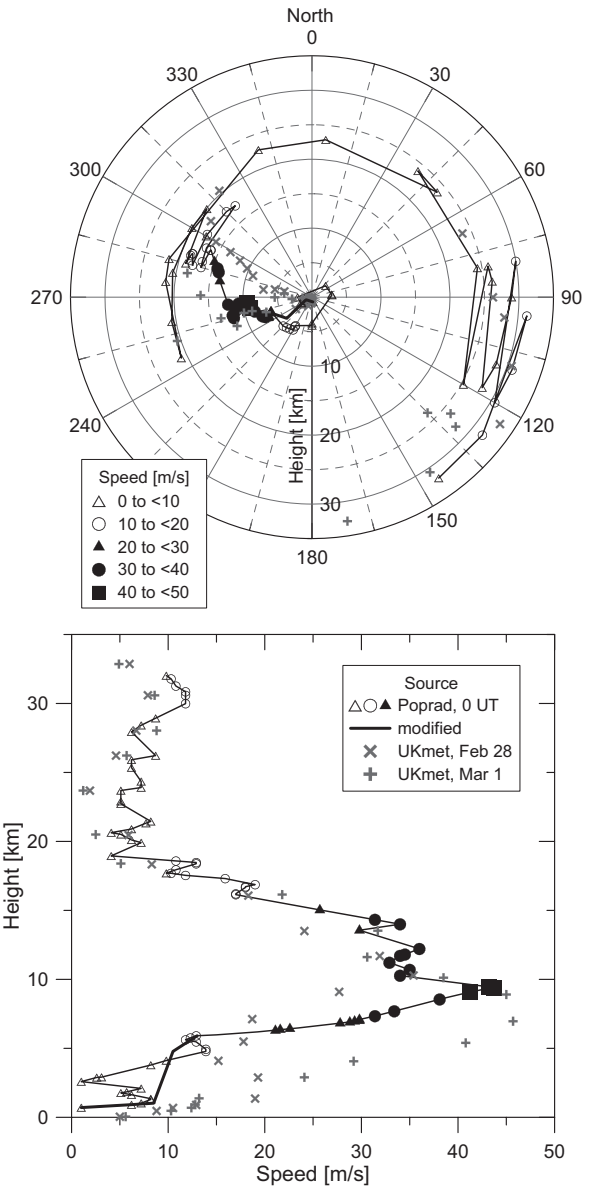

Fig. 19. Height altitude wind profile from different sources: Poprad radiosonde at 0 UT, March 1 (taken from University of Wyoming, http://weather.uwyo.edu/upperair/sounding.html) and UK MetOffice global model for coordinates 21.09375°E, 48.5625°N and time 12 UT of both February 28 and March 1 (Met Office et al. 2006). The manually modified Poprad wind for heights 0–6 km is shown as well. The upper polar plot gives wind direction as a function of height. The lower plot gives wind speed as a function of height. Different speed categories are plotted by different symbols in the Poprad winds to provide feeling about the wind importance in the polar plot.

(altitudes up to 2.6 km) to Poprad. We therefore also tried a modification in the Poprad winds where this feature was smoothed out (given in Fig. 19 as well).

In the absence of winds, the largest meteorites would be located most downrange (in the direction of

flight) and the smallest ones most uprange. As the strongest winds were in the direction almost aligned with the bolide flight, and the winds affect small meteorites much more than the large ones, the predicted strewn filed has a narrow U shape with the largest and the smallest meteorites both located downrange and the medium masses uprange. The meteorite position is also affected by the height of its separation from a larger body. For a given mass, fragments born at greater heights are located more uprange.

The modified Poprad winds provided the best agreement with the actual strewn field (Fig. 18b). There are more discrepancies for the directly measured Poprad winds (Fig. 18a). Small meteorites are expected also in the western part (longitudes around 21.13°), where they were not found, and no medium-sized meteorites are expected at around 21.18°, where a number of them were found. But even for the modified winds, the agreement is not perfect. Medium-sized and some relatively large meteorites were spread over a much larger area than expected. As far as we know, the outliers do not have any special shapes, so that aerodynamic lift is unlikely to be responsible for this deviation. It seems that the atmospheric fragmentation process was more complex and probably more violent than modeled here. Some fragments apparently received large impulses in various directions and some may have been born at large heights. We also note that some of the outliers were reported by private collectors and their coordinates could not be verified by us.

Also, the separation, 1.4 km, of the two largest recovered meteorites of similar mass is not well understood. The 2.17 kg meteorite is not fully covered by the fusion crust, so it may have been part of a larger piece until the terminal stages of the dark flight. That is why we considered the 8 kg fragment to escape from the fragmentation at the height of 21.5 km. If this was the case, one large meteorite may remain unrecovered. Still, this effect can explain only part of the separation of the two 2 kg meteorites. Note also that the crossing of the speed of sound at the height of 13 km, as suggested by seismic data, corresponds better to 2 kg meteorites separated at the height of 21.5 km. An 8 kg piece would reach the speed of sound at 11 km. So, it is possible that the missing fusion crust was caused by removal of only a small part of the mass and the separation of the two 2 kg meteorites was caused by an effect other than mass sorting, e.g., gaining impulses to opposite directions during the break up at 21.5 km.

Comparison with the Position of the Dust Cloud

We did not attempt to compute the position of the dust cloud photographed on the morning of March 1 because the cloud was so extended that the computation would be difficult. As the wind changed from westerly to easterly at 25 km (Fig. 19), the fact that the cloud moved to the west means that the observed dust was deposited into the atmosphere at heights above 25 km. Our rough estimate is that the cloud moved by about 180 km in the direction 280° within 6.75 h after the bolide. This movement requires wind direction approximately 100° and speed 7–8 m s^{-1}, both consistent with the winds at heights 25–33 km. In this height interval, several fragmentations occurred according to our model.

Comparison of Bolide Energy with Infrasonic Data

The initial meteoroid mass inferred from the light curve, 3500 kg, gives the initial bolide energy of 4×10^{11} J, i.e., 0.10 kT TNT, but with a large uncertainty by a factor of three due to the uncertainty in the absolute calibration of the light curve. Infrasonic data can provide an independent assessment of the bolide energy. Because of the large average wind speeds between the bolide and each receiver (as shown in Table 3) we expect energy estimates based on amplitude measurements, which require significant wind corrections, to be less accurate than those using the dominant signal period (see ReVelle [1976] for a detailed discussion of this issue). In fact, in the case of Košice the winds are exceptionally strong; among the 70+ bolides infrasonically described by Ens et al. (2012), less than 10% had wind corrections this strong or stronger. As a result, amplitude-related estimates of the total energy for the Košice bolide have standard deviations as large as or larger than the actual energy estimate—we consider these unreliable. To estimate the source energy we have measured the period at maximum amplitude of the bolide signal at each infrasound station and then applied a correction for the expected Doppler wind shift following Morse and Ingard (1987) to arrive at the final set of best estimates for period at each station shown in Table 3. The resulting energy estimates using the single station yield relation from Ens et al. (2012), which is basically identical to the AFTAC period-yield relationships used in earlier works (ReVelle 1997), yields an average source energy estimate of 0.19 ± 0.04 kT, very similar to that found using the multistation averaged period-yield relation of Ens et al. (2012), which gives 0.18 kT.

Ray-tracing from the bolide trajectory to each station using the observed airwave time delay as a discriminator among possible source heights, suggests that the signals at all stations were produced at heights between approximately 45–60 km along the bolide path. The ray deviations from these heights to several stations, particularly IS26, are significantly nonballistic,

Table 7. Geocentric radiant and heliocentric orbit of Košice meteoroid (J2000.0).

Geocentric radiant	
Right ascension	$\alpha_G = 114.3° \pm 1.7°$
Declination	$\delta_G = +29.0° \pm 3.0°$
Velocity	$v_G = 10.3 \pm 0.5$ km s^{-1}
Heliocentric orbit	
Semimajor axis	$a = 2.71 \pm 0.24$ AU
Eccentricity	$e = 0.647 \pm 0.032$
Perihelion distance	$q = 0.957 \pm 0.004$ AU
Aphelion distance	$Q = 4.5 \pm 0.5$ AU
Argument of perihelion	$\omega = 204.2 \pm 1.2°$
Longitude of ascending node	$\Omega = 340.072 \pm 0.004°$
Inclination	$i = 2.0 \pm 0.8°$

suggesting that acoustic radiation may have been generated by a point source detonation in this height interval. Indeed, significant fragmentation was found to start at the height of 57 km (Table 5; Fig. 15). Consequently, our estimates of the initial bolide energy from period measurements alone are larger than the true source energy. We can therefore conclude that the bolide energy of 0.1 kT or somewhat larger is in agreement with both the light curve and the infrasound analysis. The radiated energy was about 0.0025 kT.

THE PREATMOSPHERIC ORBIT

The preatmospheric orbit of the meteoroid was computed by the standard method (Ceplecha 1987) from the bolide radiant and velocity. The orbit is given in Table 7 and plotted in Fig. 20. The perihelion distance of 0.96 AU was derived with relatively high precision. The semimajor axis and, consequently, aphelion distance and eccentricity were more difficult to determine as they were very sensitive to the determination of the bolide initial velocity. The uncertainty of ± 0.3 km s^{-1} in initial velocity transforms into an uncertainty of ± 0.5 AU in aphelion distance. The resulting aphelion distance of 4.5 ± 0.5 AU is larger than for any of the 15 previously determined orbits of meteorites (see e.g., table 1 of Popova et al. [2011] and table 1 of Brown et al. [2011] and Spurný et al. [2011]); the second largest being Park Forest with 4.26 ± 0.38 AU (Brown et al. 2004). Within the limits of error, the Košice orbit may even touch the orbit of Jupiter (Fig. 20). Otherwise, the orbit was not exceptional, with low inclination and perihelion close to the orbit of the Earth.

The uncertainty in semimajor axis put the orbit close to the strong 3/1 mean motion resonance with Jupiter on one side and to the 5/2 or 7/3 resonances on the other side, and even closer to the weaker 8/3 resonance. We have numerically investigated the nominal orbit of the Košice meteorite and also 75 clones

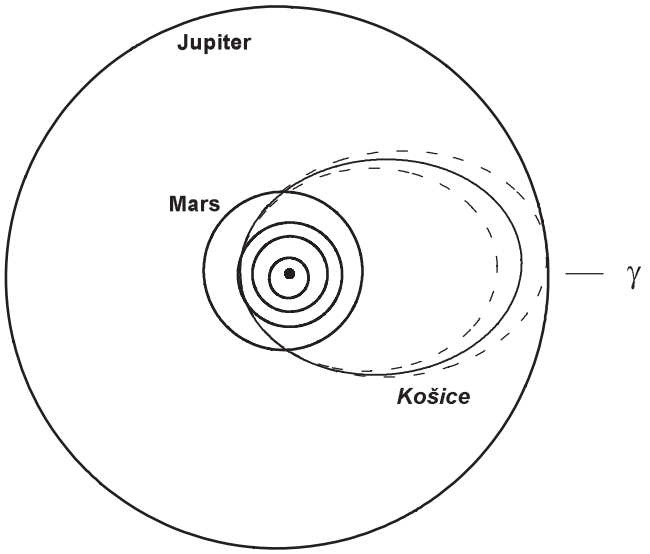

Fig. 20. Projection of the Košice meteoroid orbit into the plane of ecliptic. The dashed lines denote the limits of the orbit within one standard deviation. Orbits of planets Mercury to Jupiter and the direction to the vernal equinoctial point are also shown.

from the narrower uncertainty interval close to the nominal orbit by using the Bulirsch-Stoer algorithm from the package Mercury 6 (Chambers 1999). In the model, the planets Mercury through Neptune were considered as perturbing bodies, while the Earth and Moon were treated separately. We included the four most significantly influencing asteroids: Ceres, Pallas, Vesta, and Hygiea (Galád 2002). The backward integration period was 100,000 yr unless clear divergence in behavior was noted on a shorter time scale.

The nominal orbit of the Košice meteorite remained inside Jupiter's orbit during the interval of integration. The semimajor axis exhibited only small variations from 2.75 to 2.45 AU, the eccentricity and inclination showed much larger changes, from 0.65 to 0.97 and from 2 to 14°, respectively.

Generally, the orbits of clones were not very stable. About 25% of the cloned orbits had aphelia smaller than Jupiter's orbit during the whole investigated interval. Moreover, about 27% of the clones reached orbits with semimajor axes larger than 35 AU during the investigated time frame. As expected, the Earth and Venus were the most prominent perturbing bodies for orbital evolution, which caused close approaches to Jupiter with corresponding dramatic orbital changes.

The orbital evolution of the nominal orbit of the meteorite as well as of several clones representing typical behavior of the cloned orbits is depicted in Fig. 21. The graph of semimajor axis contains the nominal orbit as representative of the evolution of 19 clones in the range from 2.2 to 3.2 AU, the other two

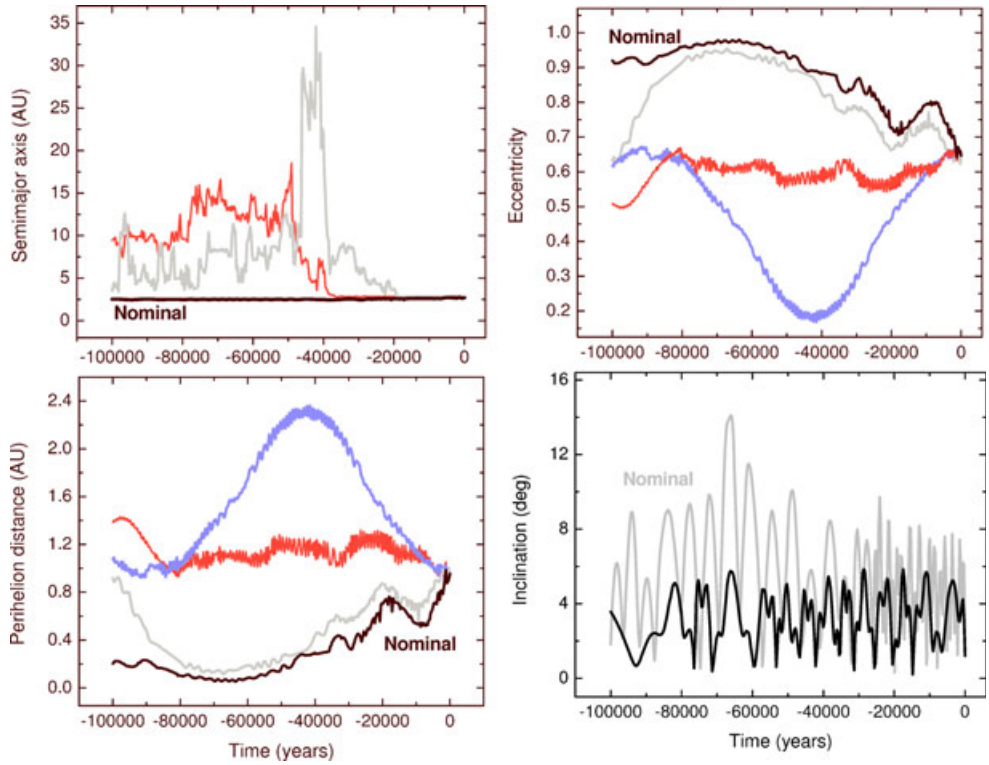

Fig. 21. Orbital evolution of the nominal orbit of the meteoroid Košice and of one to three clones representing the typical behavior of the cloned orbits during the last 100,000 yr. In the graph of semimajor axis, the nominal orbit illustrates the evolution of 19 clones with a in the range from 2.2 to 3.2 AU, the other two curves represent 11 other stable orbits with $a < 35$ AU. The graphs of eccentricity, inclination, and perihelion distance contain only representatives of the 19 clones with $a < 5$ AU.

curves are examples of another 11 stable orbits with $a < 35$ AU during the last 100,000 yr. The graphs of eccentricity, inclination, and perihelion distance in Fig. 21 contain only representatives of the aforementioned 19 clones. Most of these orbits have eccentricities in the interval 0.5–0.8 and inclinations from 2 to 8°. In all graphs, a long periodic influence of Jupiter can be seen, changing the eccentricities from 0.2 to nearly 1.0 and inclinations, to almost 15°.

Three Apollo type asteroids, namely 2002 CX58, 2009 BC11, and 2000 DO8, have similar osculating orbits to the Košice meteorite with the Southworth-Hawkins D criterion (Southworth and Hawkins 1963) $D_{SH} \leq 0.10$. They might have some connection to the meteorite but a more detailed study would be needed to draw any conclusions.

DISCUSSION

As bad weather prevented regular observation of the Košice meteorite fall, we were lucky in obtaining three casual videos of the bolide. The spatial distribution of video sites was not ideal; nevertheless, the videos enabled us, after careful calibration, to reconstruct the bolide trajectory, velocity, and orbit, and to compute meteorite fall area. The precision of the orbit is relatively low but is comparable to some other similar cases reconstructed from casual records, e.g., Park Forest. Fortunately, the large number of fallen meteorites made the meteorite recovery relatively easy. Finally, the radiometers of the European Network fireball cameras, although located far from the bolide and obscured by thick clouds, recorded the bolide light curve and enabled us to reconstruct the bolide brightness and the fragmentation history of the meteoroid in the atmosphere.

With a maximum brightness of −18 mag, the Košice bolide classifies into the superbolide category (Ceplecha et al. 1999). The Košice meteoroid, with an initial mass of about 3500 kg and diameter of 1.25 m, belongs to the population of relatively massive meteorite-producing bodies. The kinetic energy at the entry into the atmosphere was almost 0.1 kt TNT (1 kt TNT = 4.185×10^{12} J). The meteoroid was a stony ordinary chondrite of type H5. All these parameters would suggest that a large meteorite, of the order of several tens of kilograms, could reach the ground. However, this was not the case. The decisive factor was the mechanical strength of the meteoroid. This quantity

varies from case to case, even for bodies of the same mineralogical type (Popova et al. 2011). Košice was a weak meteoroid which fragmented heavily under the dynamic pressure of approximately 1 MPa, at the height of approximately 38 km. In this respect, it resembled the much more massive meteoroids Tagish Lake (Brown et al. 2002) and Almahata Sitta (Borovička and Charvát 2009; Jenniskens et al. 2009), which also disrupted catastrophically at similar pressures. Both of them, however, were of different mineralogical types (carbonaceous chondrite and ureilite, respectively). Both of them also disrupted more severely, terminating the bolide at approximately 30 km height and dropping only small meteorites (<<1 kg) to the ground. In contrast, parts of Košice were strong enough and although they fragmented further, the maximum encountered dynamic pressure approached 6 MPa, a value quite comparable with other ordinary chondrite falls (Popova et al. 2011).

The reason for this severe fragmentation at 1 MPa and even as low as 0.1 MPa must have been, as in other similar cases, prefragmentation of the meteoroid from collisions in interplanetary space. The meteoroid was probably full of internal fractures and cracks, leaving only a small part of the volume relatively strong. In fact, Peekskill may have been a similar case, as it also fragmented heavily at low pressures (Ceplecha et al. 1996), but the extremely shallow trajectory of Peekskill makes a direct comparison difficult. Morávka disrupted initially at low pressure, but most of the mass continued as still relatively large fragments of strength approaching 5 MPa (Borovička and Kalenda 2003). We plan to use our improved meteoroid fragmentation model and apply it to some other meteorite falls with good light curve data and to selected important bolides to facilitate more comparison.

The heliocentric orbit of Košice was characterized by a low inclination (2°) and relatively large semimajor axis (2.7 AU), which places the likely origin of the body in the central main asteroid belt near the 8:3 main motion resonance with Jupiter. According to Bottke et al. (2002), 24% of near-Earth objects come from the central Main Belt.

Acknowledgments—We thank G. Vass, D. Fazzi, T. Meszlényi, and I. Asztalos for providing video records of the bolide and allowing us to take calibration images at their homes. We acknowledge all the MCSE members helping us during the calibration of the videos. We are obliged to M. Zivcić, R. Maurers, P. Mónus, P. Moczo, and A. Cipciar for providing the seismic data and J. Zedník for their conversion. Our thanks go to all who participated in meteorite searches, in particular Z. Bartoš, M. Bodnárová, D. Búzová, D. Čapek, P. Delinčák, T. Dobrovodský, Š. Gajdoš, S. Kanianský, J. Koza, Z. Krišandová, T. Krejčová, A. Kučera, Z. Mimovičová, J. Nedoroščík, J. Petržala, E. Schunová, M. Šebeň, J. Šilha, M. Škreka, D. Tomko, P. Vereš, J. Világi, and P. Zigo. We thank D. Heinlein, Z. Tyminski, J. Woreczko, and T. Gulon for information about nonofficial meteorite finds. This study was supported by GAČR grants no. P209/11/1382 and 205/08/0411, SRDA contract no. APVV-0516-10, and VEGA grants no. 1/0636/09 and 2/0022/10 as well as the institutional research plan AV0Z10030501.

Editorial Handling—Dr. Pavel Povinec

REFERENCES

Borovička J. 1990. The comparison of two methods of determining meteor trajectories from photographs. *Bulletin of the Astronomical Institutes of Czechoslovakia* 41:391–396.

Borovička J. and Charvát Z. 2009. Meteosat observation of the atmospheric entry of 2008 TC_3 over Sudan and the associated dust cloud. *Astronomy & Astrophysics* 507:1015–1022.

Borovička J. and Kalenda P. 2003. The Morávka meteorite fall: 4. Meteoroid dynamics and fragmentation in the atmosphere. *Meteoritics & Planetary Science* 38:1023–1043.

Borovička J., Spurný P., and Koten P. 2007. Atmospheric deceleration and light curves of Draconid meteors and implications for the structure of cometary dust. *Astronomy & Astrophysics* 473:661–672.

Bottke W. F., Morbidelli A., Jedicke R., Petit J.-M., Levison H. F., Michel P., and Metcalfe T. S. 2002. Debiased orbital and absolute magnitude distribution of the near-Earth objects. *Icarus* 156:399–433.

Brown P. G., ReVelle D. O., Tagliaferri E., and Hildebrand A. R. 2002. An entry model for the Tagish Lake fireball using seismic, satellite and infrasound records. *Meteoritics & Planetary Science* 37:661–675.

Brown P., Pack D., Edwards W. N., Revelle D. O., Yoo B. B., Spalding R. E., and Tagliaferri E. 2004. The orbit, atmospheric dynamics, and initial mass of the Park Forest meteorite. *Meteoritics & Planetary Science* 39:1781–1796.

Brown P., McCausland P. J. A., Fries M., Silber E., Edwards W. N., Wong D. K., Weryk R. J., Fries J., and Krzeminski Z. 2011. The fall of the Grimsby meteorite—I: Fireball dynamics and orbit from radar, video, and infrasound records. *Meteoritics & Planetary Science* 46:339–363.

Ceplecha Z. 1987. Geometric, dynamic, orbital and photometric data on meteoroids from photographic fireball networks. *Bulletin of the Astronomical Institutes of Czechoslovakia* 38:222–234.

Ceplecha Z. and ReVelle D. O. 2005. Fragmentation model of meteoroid motion, mass loss, and radiation in the atmosphere. *Meteoritics & Planetary Science* 40:35–50.

Ceplecha Z., Brown P., Hawkes R. L., Wertherill G., Beech M., and Mossman K. 1996. Video observations, atmospheric path, orbit and fragmentation record of the fall of the Peekskill meteorite. *Earth, Moon, and Planets* 72:395–404.

Ceplecha Z., Borovička J., Elford G. W., ReVelle D. O., Hawkes R. L., Porubčan V., and Šimek M. 1998. Meteor phenomena and bodies. *Space Science Reviews* 84:327–471.

Ceplecha Z., Spalding E. R., Jacobs C., Revelle D. O., Tagliaferri E., and Brown P. 1999. Superbolides. In *Meteoroids 1998*, edited by Baggaley W. J. and Porubčan V. Bratislava, Slovakia: Astronomical Institute, Slovak Academy of Sciences. pp. 37–54.

Chambers J. E. 1999. A hybrid symplectic integrator that permits close encounters between massive bodies. *Monthly Notices of the Royal Astronomical Society* 304: 793–799.

Christie D. R. and Campus P. 2010. The IMS infrasound network: Design and establishment of infrasound stations. In *Infrasound monitoring for atmospheric studies*, edited by Le Pichon A., Blanc E., and Hauchecorne A. Dordrecht: Springer. pp. 27–73.

Edwards W. N. 2010. Meteor generated infrasound: Theory versus observations. In *Infrasound monitoring for atmospheric studies*, edited by Le Pichon A., Blanc E., and Hauchecorne A. Dordrecht: Springer. pp. 361–414.

Edwards W. N. and Hildebrand A. R. 2004. SUPRACENTER: Locating fireball terminal bursts in the atmosphere using seismic arrivals. *Meteoritics & Planetary Science* 39:1449–1460.

Edwards W. N., Brown P. G., and ReVelle D. O. 2006. Estimates of meteoroid kinetic energies from observations of infrasonic airwaves. *Journal of Atmospheric and Solar-Terrestrial Physics* 68:1136–1160.

Ens T. A., Brown P. G., Edwards W. N., and Silber E. A. 2012. Infrasound production by bolides: A global statistical study. *Journal of Atmospheric and Solar-Terrestrial Physics* 80:208–229, doi:10.1016/j.jastp. 2012.01.018.

Galád A. 2002. Asteroid encounters suitable for mass determinations. *Astronomy & Astrophysics* 391:1115–1122.

Gritsevich M. and Koschny D. 2011. Constraining the luminous efficiency of meteors. *Icarus* 212:877–884.

Jenniskens P., Shaddad M. H., Numan D., Elsir S., Kudoda A. M., Zolensky M. E., Le L., Robinson G. A., Friedrich J. M., Rumble D., Steele A., Chesley S. R., Fitzsimmons A., Duddy S., Hsieh H. H., Ramsay G., Brown P. G., Edwards W. N., Tagliaferri E., Boslough M. B., Spalding R. E., Dantowitz R., Kozubal M., Pravec P., Borovička J., Charvat Z., Vaubaillon J., Kuiper J., Albers J., Bishop J. L., Mancinelli R. L., Sandford S. A., Milam S. N., Nuevo M., and Worden S. P. 2009. The impact and recovery of asteroid 2008 TC_3. *Nature* 458:485–488.

Kohout T., Havrila K., Tóth J., Husárik M., Gritsevich M., Britt D., Borovička J., Spurný P., Igaz A., Kornoš L., Vereš P., Koza J., Kučera A., Zigo P., Gajdoš Š., Világi J., Čapek D., Krišandová Z., Tomko D., Šilha J., Schunová E., Bodnárová M., Búzová D., and Krejčová T. Forthcoming. Density, porosity and magnetic susceptibility of the Košice meteorites and homogeneity of H chondrite showers. *Meteoritics & Planetary Science*.

Met Office [Swinbank R., O'Neill A., Lorenc A. C., Ballard S. P., Bell R. S., Ingleby N. B., Andrews P. L. F., Barker D. M., Bray J. R., Clayton A. M., Dalby T., Li D., Payne T. J., Saunders F. W., Macpherson B., Cullen M. J. P., Davies T., and Mawson M. H.]. Stratospheric Assimilated Data [Internet]. NCAS British Atmospheric Data Centre, 2006. Last accessed March 17, 2010. Available from http://badc.nerc.ac.uk/view/badc.nerc.ac.uk__ATOM__dataent_ASSIM

Morse P. M. and Ingard K. U. 1987. *Theoretical acoustics*. Princeton, New Jersey: Princeton University Press. pp. 699–700.

Popova O., Borovička J., Hartmann W. K., Spurný P., Gnos E., Nemtchinov I., and Trigo-Rodríguez J. 2011. Very low strengths of interplanetary meteoroids and small asteroids. *Meteoritics & Planetary Science* 46:1525–1550.

Revelle D. O. 1976. On meteor-generated infrasound. *Journal of Geophysical Research* 81(7):1217–1230.

ReVelle D. O. 1997. Historical detection of atmospheric impacts by large bolides using acoustic-gravity waves. *Annals of the New York Academy of Sciences* 822:284–302.

ReVelle D. O. and Ceplecha Z. 2001. Bolide physical theory with application to PN and EN fireballs. Proceedings of the Meteoroids 2001 Conference, ESA SP-495. pp. 507–512.

ReVelle D. O., Brown P. G., and Spurný P. 2004. Entry dynamics and acoustics/infrasonic/seismic analysis for the Neuschwanstein meteorite fall. *Meteoritics & Planetary Science* 39:1605–1626.

Southworth R. B. and Hawkins G. S. 1963. Statistics of meteor streams. *Smithsonian Contributions to Astrophysics* 7:261–285.

Spurný P., Borovička J., and Shrbený L. 2007. Automation of the Czech part of the European Fireball Network: Equipment, methods and first results. In *Near Earth objects, our celestial neighbors: Opportunity and risk*, Proceedings of IAU Symposium 236, edited by Valsecchi G. B., Vokrouhlický D., and Milani A. Cambridge, UK: Cambridge University Press. pp. 121–130.

Spurný P., Borovička J., Kac J., Kalenda P., Atanackov J., Kladnik G., Heinlein D., and Grau T. 2010. Analysis of instrumental observations of the Jesenice meteorite fall on April 9, 2009. *Meteoritics & Planetary Science* 45:1392–1407.

Spurný P., Bland P. A., Shrbený L., Towner M. C., Borovička J., Bevan A. W. R., and Vaughan D. 2011. The Mason Gully meteorite fall in SW Australia: Fireball trajectory and orbit from photographic records (abstract #5101). *Meteoritics & Planetary Science* 46:A220.

Spurný P., Bland P. A., Shrbený L., Borovička J., Ceplecha Z., Singelton A., Bevan A. W. R., Vaughan D., Towner M. C., McClafferty T. P., Toumi R., and Deacon G. 2012. The Bunburra Rockhole meteorite fall in SW Australia: fireball trajectory, luminosity, dynamics, orbit, and impact position from photographic and photoelectric records. *Meteoritics & Planetary Science* 47:163–175.

Stöffler D., Keil K., and Scott E. R. D. 1991. Shock metamorphism of ordinary chondrites. *Geochimica et Cosmochimica Acta* 55:3845–3867.

Tóth J., Kornoš L., Vereš P., Šilha J., Kalmančok D., Zigo P., and Világi J. 2011. All-sky video orbits of Lyrids 2009. *Publications of the Astronomical Society of Japan* 63:311–314.

SUPPORTING INFORMATION

Additional supporting information may be found in the online version of this article:

Data S1. Positions of Košice bolide from video records.